



# Analysis of the Microscopic Evolution of Rock Damage Based on Real-Time Nuclear Magnetic Resonance

Jing Bi<sup>1</sup> · Lin Ning<sup>1</sup> · Yu Zhao<sup>1</sup> · Zhijun Wu<sup>2</sup> · Chaolin Wang<sup>1</sup>

Received: 16 July 2022 / Accepted: 15 January 2023 / Published online: 30 January 2023  
© The Author(s), under exclusive licence to Springer-Verlag GmbH Austria, part of Springer Nature 2023

## Abstract

Under the action of a load, internal pores and cracks expand, and irreversible plastic deformations occur. Compared with conventional rock mechanics tests, nuclear magnetic resonance (NMR) can characterize the size and distribution of pores at the microscopic scale. In this study, a series of low-confining-stress triaxial compression tests were performed on different types of sandstone samples using real-time T2-weighted NMR spectra and imaging. It was found that the area of macropores in sandstone significantly increased only during the initial loading stage, but played an opposite role in the damage evolution process. This phenomenon is contrary to our expectations and provides a new basis for understanding the evolution of damage in rocks. Furthermore, during the linear deformation stage, the number of pores and mesopores increased, whereas the number of macropores decreased. A damage model based on the NMR results is proposed. The value of  $D_n$  sharply increases during the initial stage due to the expansion of pores, then decreases, and finally begins to increase again before the failure stage and until the sample fractures owing to the development of macroscopic cracks. In conclusion, the structure of micropores has a significant influence on the failure mode of sandstone rocks in low-confining-pressure triaxial compression tests.

## Highlights

- The area of macropores in sandstone significantly increased only during the initial loading stage and played an opposite role in the damage evolution process.
- During the linear deformation stage, the number of pores and mesopores increased, whereas the number of macropores decreased.
- The structure of micropores has a significant influence on the failure mode exhibited by sandstone during low-confining-pressure triaxial compression tests.

**Keywords** Different types of sandstone · Real-time T2 and MRI image measurement · Damage evolution · Fracture characteristics

## 1 Introduction

During the construction and operation of underground engineering projects, the rock mass is constantly subjected to the action of an external load, which causes damage to its

interior (Munoz and Taheri 2017; Tin and Xu 2021; Bi et al. 2022). This damage accumulates as the stress increases, adversely affecting not only the stability of the surrounding rock during construction but also the long-term operation of the underground engineering facility. In particular, when underground engineering projects are located in a relatively permeable stratum, such as sandstone, the combined action of the increased stress and groundwater flow further reduces the stability of the surrounding rock and the service life of the project, and increases the risk of construction and service engineering. Therefore, the study of real-time damage evolution of sandstones under stress loading is required (Fahimifar and Zareifard 2014).

✉ Yu Zhao  
20151601005@cqu.edu.cn

<sup>1</sup> College of Civil Engineering, Guizhou University, Guiyang 550025, China

<sup>2</sup> School of Civil Engineering, Wuhan University, Wuhan 430072, China

Sandstone is a common, porous, and brittle natural material. Under the action of load, internal pores and cracks expand, and irreversible plastic deformations occur. Therefore, sandstone characterizes by elastic-plastic damage and the rock easily accumulates damage during external loading, resulting in a nonlinear stress-strain triaxial loading curve. Consequently, triaxial loading is a reasonable and effective loading method for studying the damage evolution of sandstones (David et al. 2012; Sun et al. 2017a).

Researchers have studied the pore structure and fracture evolution of rock materials under loading and other external environmental conditions using many different methods, including scanning electron microscopy (SEM), micro computed tomography (CT), mercury intrusion porosimetry (MIP) (De Castro et al. 2020), mercury injection (Zhang et al. 2017; Zuo et al. 2007; Sun et al. 2017b), acoustic emission (AE) (Liu et al. 2015; Rodriguez et al. 2016), and nuclear magnetic resonance (NMR) (Cheng et al. 2021; Huang et al. 2021). The development of macro- and micro-fractures as rock damage evolves has been extensively studied through experimental and theoretical research based on these testing methods. AE generates transient elastic waves by the rapid release of local strain energy, which allows for global, non-destructive, real-time, and extremely frequent monitoring, making it a good tool for identifying predictors (or more generally, potential precursors) of failure in brittle rocks (Zhang and Zhou 2020a, b). The MIP method can help detect damage in coal samples (Zhao et al. 2022). CT can produce images of the pores and fractures, but usually at a resolution of more than 1  $\mu\text{m}$  (although industrial CT can achieve higher resolution, its cost is a disadvantage) (Meng et al. 2019). Furthermore, fine pore changes and transgranular failure during loading can be observed using SEM (Fang et al. 2018).

Compared with conventional rock mechanics tests, NMR can characterize the size and distribution of pores at the microscopic scale. Moreover, NMR offers a higher precision (pores up to 0.1 nm can be detected) and better economy and convenience than other non-destructive testing methods. In recent years, many researchers have examined the pore structure and physical properties (permeability and porosity) of rocks using conventional NMR. However, the use of NMR to detect in real-time the evolution of pores and fractures as stress increases is rare because of the limitations of the NMR equipment. Therefore, the way pores change and transform under loading conditions is still unclear (Li et al. 2020; Jin et al. 2020; Meng et al. 2021; Wei et al. 2019; Zhao et al. 2020), despite the mechanism of rock pore evolution being fundamental to understanding the damage and failure process of rocks. Consequently, to clearly reveal the evolution law of pores and fractures with stress, we propose using real-time NMR based on a triaxial experimental device, through which the damage evolution process of rocks can

be examined from a microscopic point of view. Thus, the entire process of rock damage initiation, evolution, and failure can be determined and the mechanism governing damage in rocks can be revealed. This is of great significance for the safety of underground engineering projects. In the proposed method, pore size distribution (PSD) is characterized by the intensity (amplitude, peak area, and continuity) of the T2-weighted NMR signals (Frosch et al. 2000), so that an increasing NMR signal strength indicates a larger number of pores (Fang et al. 2016). The longer the transverse relaxation time (T2), the larger the pores and the smaller the surface volume ratio (Dunn et al. 2002). In addition, existing studies have shown that coal pores can be divided into three types: micropores, mesopores, and macropores (Tang et al. 2016; Westphal et al. 2005). In this study, the change of the micropores, mesopores, and macropores were determined during the loading process and the rock damage evolution mechanism was analyzed based on a real-time NMR test. Finally, the changes in the pore structure, from rock damage to failure, were determined, thus providing mechanical guidance for improving the safety of underground engineering facilities.

## 2 Sample Materials and Testing Equipment

### 2.1 Nuclear Magnetic Resonance (NMR) Principle

NMR has been recently used as an effective method for studying the pore structure and damage evolution in rocks. This phenomenon is based on the relaxation displayed by charged spin hydrogen nuclei of fluids within rock pores when exposed to constant magnetic (CM) and radio frequency (RF) magnetic fields (Li et al. 2020; Jin et al. 2020; Meng et al. 2021; Weng et al. 2021; Zhao et al. 2018; Zhou et al. 2021). When the saturated rock specimen is placed in the CM field, the hydrogen nuclei of the water in the specimen are magnetized and gain a magnetization vector. In such a condition, the application of an RF field triggers NMR. Owing to certain quantum mechanics properties, when the RF field stops acting, the hydrogen nuclei relax. This relaxation produces a signal, whose variation in amplitude can be described by the longitudinal and transverse relaxation times, T1 and T2, respectively (Carette and Staquet 2016; Cai et al. 2013). In NMR tests, owing to its high detection speed, the T2 spectrum is generally used to describe the distribution of pores in rocks. This method is fast, non-destructive, informative, and has a wide measurement range (Zhai et al. 2015) (Fig. 1). The amplitude of the T2 distribution reflects the number of pores of a given size. The larger the amplitude, the greater the number of pores. Therefore, the NMR technique is advantageous for analyzing the pore structure and damage evolution process

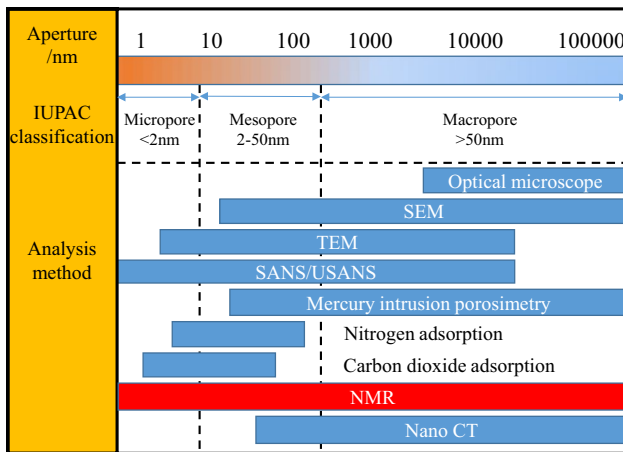


Fig. 1 Rock pore classification and research methods (Li et al. 2020)

of porous rock materials. It can reveal the entire process, from damage to failure.

### 2.2 Sandstone Sample Preparation

Samples of gray fine sandstone from the Tongchuan area, medium-coarse-grained sandstone from the Jiangsu area, and red coarse sandstone from the Guizhou area were used for testing in this study. The sandstone samples were cylindrical, with a diameter of 25 mm and a height of 50 mm. The rock samples were compact, homogenous, isotropic, and free of fractures and macrocracks. The names, densities, and porosities of the six sandstone samples prepared are listed in Table 1.

### 2.3 Experimental Equipment

The experimental setup used to investigate pore development and mechanical properties of the rock samples is shown in Fig. 2. A MacroMR-150H-I low-field NMR system (Niumag Corporation, Suzhou, China) was used to obtain T2-weighted NMR spectra and images during the triaxial

compression experiments. The low-field NMR system consisted of a drying oven, NMR device, and triaxial cell, as well as loading, water supply, temperature, and computerized data-acquisition units. The NMR device had a maximum detection range of 150 mm in diameter and 100 mm in length, a magnetic field strength of 0.3 T, and a resonance frequency of 12 MHz. Moreover, it is comprised of an RF coil and a gradient unit that can provide a maximum gradient intensity of 0.15 T/m in the X, Y, and Z directions. To maintain the stability of the device, all the NMR tests were performed at a constant temperature of 32 °C.

The triaxial cell was made of non-metallic polymer synthetic materials. Three pressure pumps with maximum capacities of 40, 100 and 40 MPa were used to apply the confining, axial load, and pore pressures, respectively. In addition, the testing system was provided with a temperature unit that can control the experimental temperature in the range of -20 to 100 °C, using fluorinated liquid and an oil bath to respectively lower or increase the temperature.

### 2.4 Experimental Procedure

Before testing, the sandstone samples were first cooled for 10 h, then vacuum-saturated for 24 h, and finally placed in the triaxial cell of the NMR system after reaching 100% saturation. During the test, first, in situ NMR scans of the sandstone samples were performed. Then, the confining and pore pressures were increased to a predetermined value at a rate of 0.5 MPa/min. Subsequently, axial loading was applied in increments of 5 MPa until reaching 10 MPa and thereafter in increments of 2 MPa at a rate of 0.5 MPa/min; each stress level was maintained for 60 s to perform in situ NMR scans to obtain pore growth, damage evolution and corresponding MRI images. Loading continued until the sample failed. All six sandstone samples (F-1, F-2, M-1, M-2, C-1, and C-2) were identically prepared and loaded under the same confining and pore pressures (2.0 and 1.0 MPa, respectively). The testing procedures for the three sandstone types are shown in Fig. 3.

Table 1 Basic physical properties of the sandstones

Types	Sample name	Elastic modulus (GPa)	Uniaxial strength (MPa)	Density (g/cm <sup>3</sup> )	Porosity (%)
The gray fine sandstone	F-1	0.8	24	2.481	1.27
	F-2	0.9	25	2.474	1.58
The medium-coarse-grained sandstone	M-1	2.1	36	2.193	5.79
	M-2	2.0	37	2.202	5.66
The red coarse sandstone	C-1	3.7	42	2.012	9.24
	C-2	3.9	43	2.010	9.43

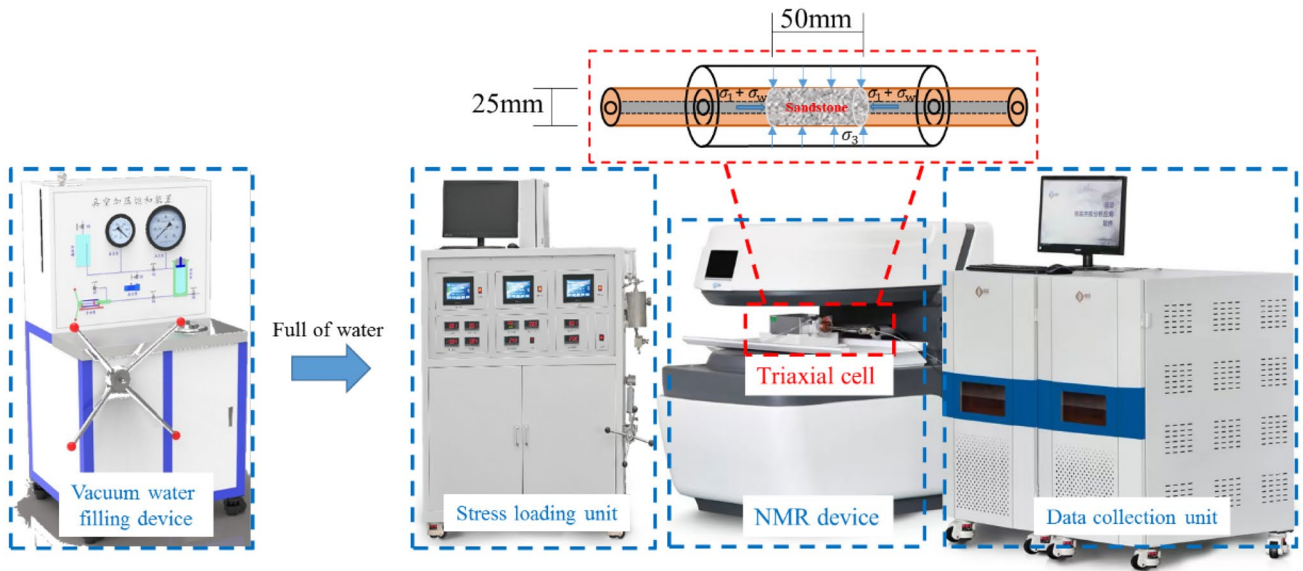


Fig. 2 Real-time loading and nuclear magnetic resonance equipment (MacroMR-150H-I low-field NMR system)

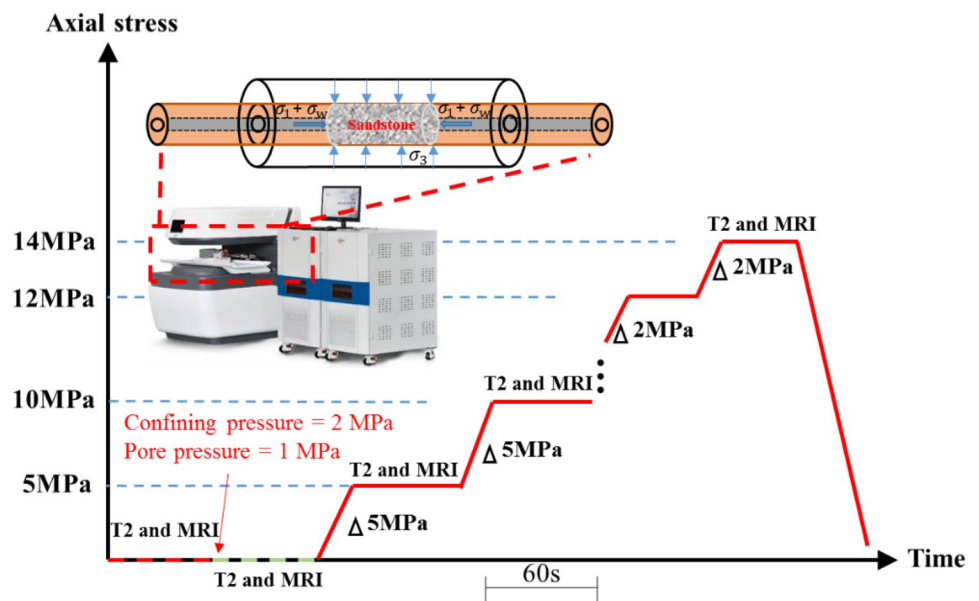
### 3 Results and Discussion

#### 3.1 Analysis of T2-Weighted Spectra

According to the relaxation mechanism of NMR, the signal emitted by the fluid in different types of pores in the rock has different relaxation times and is distributed at different positions along the time axis of the T2-weighted spectrum. The development or evolution characteristics of the damage and fractures in sandstone can be determined based on the distribution of the peak values of the T2 spectrum signals

(Li et al. 2020). The NMR signal intensity increases with the number of pores (Cai et al. 2013), and a longer T2 indicates larger pores with small large surface-to-volume ratios and vice versa (Zhai et al. 2015). The peak width of the T2 spectrum reflects the distribution of a particular type of pore, whereas the peak area reflects the number of pores of this type. In addition, the smaller the pore size, the shorter the relaxation time, and vice versa. The T2 of the fluid in a porous media can be expressed as

Fig. 3 Schematic diagram of the experimental procedures of the triaxial compression tests and real-time NMR measurements



$$\frac{1}{T_2} = \frac{1}{T_{2s}} + \frac{1}{T_{2D}} + \frac{1}{T_{2B}} \tag{1}$$

where  $T_{2s}$  is the time of surface relaxation of the rock particles,  $T_{2B}$  is the relaxation time from the liquid itself, and  $T_{2D}$  is the relaxation time caused by molecular diffusion. Considering that surface relaxation plays a decisive role, the above equation can be simplified as follows (Matteson et al. 2000):

$$\frac{1}{T_2} = \frac{1}{T_{2S}} = \frac{\rho_2 S}{V} = \rho_2 \frac{F_s}{r} \tag{2}$$

where  $\rho_2$  is the transverse surface relaxation strength,  $F_s$  is the geometric factor of the pore shape (for tubular pores,  $F_s = 2$ ), and  $r$  is the pore radius.

Although some researchers have studied the relationship between pore size and relaxation time, there are no acknowledged criteria (Zhang et al. 2017; Li et al. 2019). In this study,  $\rho_2$  in Eq. (2) was considered to be 5  $\mu\text{m/s}$  (Jia et al. 2020). The ratio of the spectrum amplitude of pores of a specific size to the spectrum amplitude of the entire specimen describes the distribution of pore sizes within the rock. Thus, the T2 spectrum can be converted into a pore size distribution under different treatments, as shown in Fig. 4. The horizontal axis represents the porosity component, and the area enclosed by the curve and the horizontal axis corresponds to the volume of pores or cracks. Based on the relaxation time, Hodot (1966) divided rock pores into micropores (< 1 ms), pores (1–10 ms), mesopores (10–100 ms), and macropores (> 100 ms).

The distribution curves derived from the T2-weighted spectra for the three types of sandstone at different loading stages are shown in Fig. 4. The T2 spectrum variation of the three different types of sandstone shows that the distributions of pore size and quantity are very different. The overall decline in NMR signal intensity varied with the fineness of

the sandstone. The location of the first peak, which corresponds to the micropores, moves to the left as coarse grain size. This indicates that among the three types of rocks, fine sandstone has the most micropores, and the pore size is smaller than that of the other two types of sandstone. Furthermore, the peak corresponding to the pores in sample F-2 was the most evident. In general, as the axial loading increased, the NMR signal intensity first slightly decreased and then increased in a nonlinear way. However, for the medium-coarse-grained sandstone and coarse sandstone, the micropore distribution did not significantly change compared with other pore size distributions. For fine sandstone, the change in pore distribution is minimal. This phenomenon indicates that the contribution of the pore structure to the damage evolution of different sandstones differs during the loading process.

In general, four stages can be identified in the stress-strain curves of the tested rock samples at the macro level: compaction, linear deformation, elastic-plastic, and post-peak stages (Bi et al. 2020; Zhou et al. 2019; Kou et al. 2021; Zheng et al. 2021; Zhao et al. 2021). However, from a micro perspective, the smaller pore structure exhibited little change or a small decreasing trend during the loading process. To distinguish the contribution of pore structure changes to the damage evolution, the change in the area of the pore spectral distribution was analyzed. The relationship between the deviatoric stress and area for different sandstones is plotted in Fig. 5. Areas A1, A2, A3, and A4 correspond to the area of micropores, pores, mesopores, and macropores, respectively. As shown in Fig. 5a, area A1 shows small fluctuations, with no significant variation with the increase in deviatoric stress. This indicates that the micropores in sandstone contribute little to rock damage during the loading process. The slight fluctuations were caused by pore compaction and slight pore increase. For the pores and mesopores, the area tended to increase with an increase in loading stress.

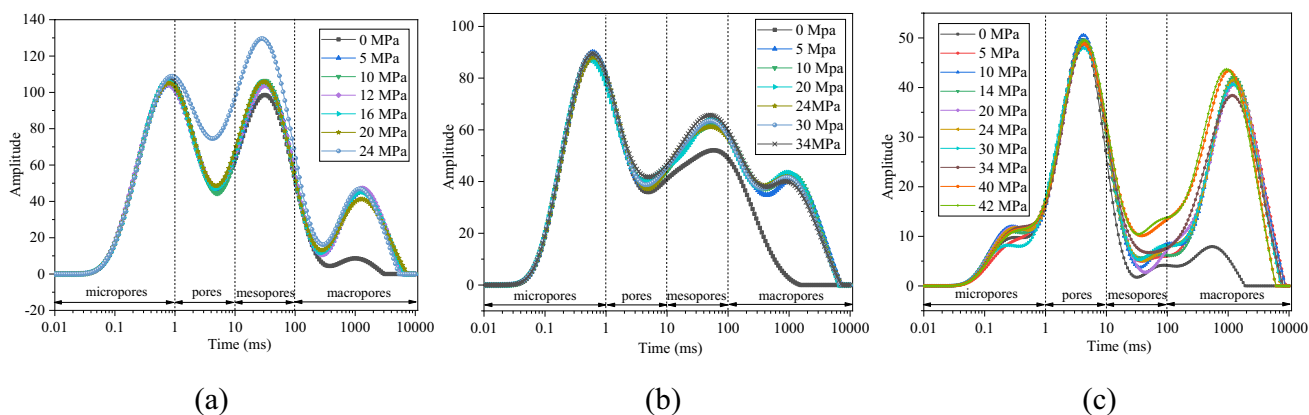


**Fig. 4** The T2 distribution variation of sandstone: **a** The T2 distribution of sample C-1; **b** The T2 distribution of sample M-1; **c** The T2 distribution of sample F-2

Especially in the failure stage, the area of the pores and mesopores in the coarse sandstone significantly increased. The increase in the area of the pores and mesopores reached 46.7% and 30.3%, respectively. However, the increments in the area of the pores and mesopores in samples M-1 and F-2 were comparatively small. The increment in sample F-2 was the smallest owing to its initial pore structure. In contrast to the other three pore conditions, the area of the macropores in the three different sandstones significantly increased under the initial loading condition and continued to decrease with increasing loading stress. This indicates that the macropores in sandstone exhibit a large increase only during the initial loading stage, but they play an opposite role in the damage evolution process. This phenomenon is contrary to our expectations and provides a new basis for understanding the evolution of damage in rocks.

### 3.2 Characteristics of Pore Change

To explain the characteristics of the pore changes described above, crack opening and propagation characteristics were introduced and analyzed. Consider a micro-body in a rock sample with length  $L$  and width  $b$  that contains an elliptical crack with half-length  $c$  and is subjected to compression  $\sigma$  in the longitudinal direction as shown in Fig. 6a. The effective Young's modulus of the micro-body can be defined as (Jaeger et al. 2007):

$$\frac{\sigma^2 bL}{2E_{eff}} = \frac{\sigma^2 bL}{2E} + \Delta W \tag{3}$$

where  $bL$  is the volume of the body,  $E$  is Young's modulus of the unfractured body, and  $\Delta W$  is the excess energy stored in the rock body owing to the presence of fractures or damage.

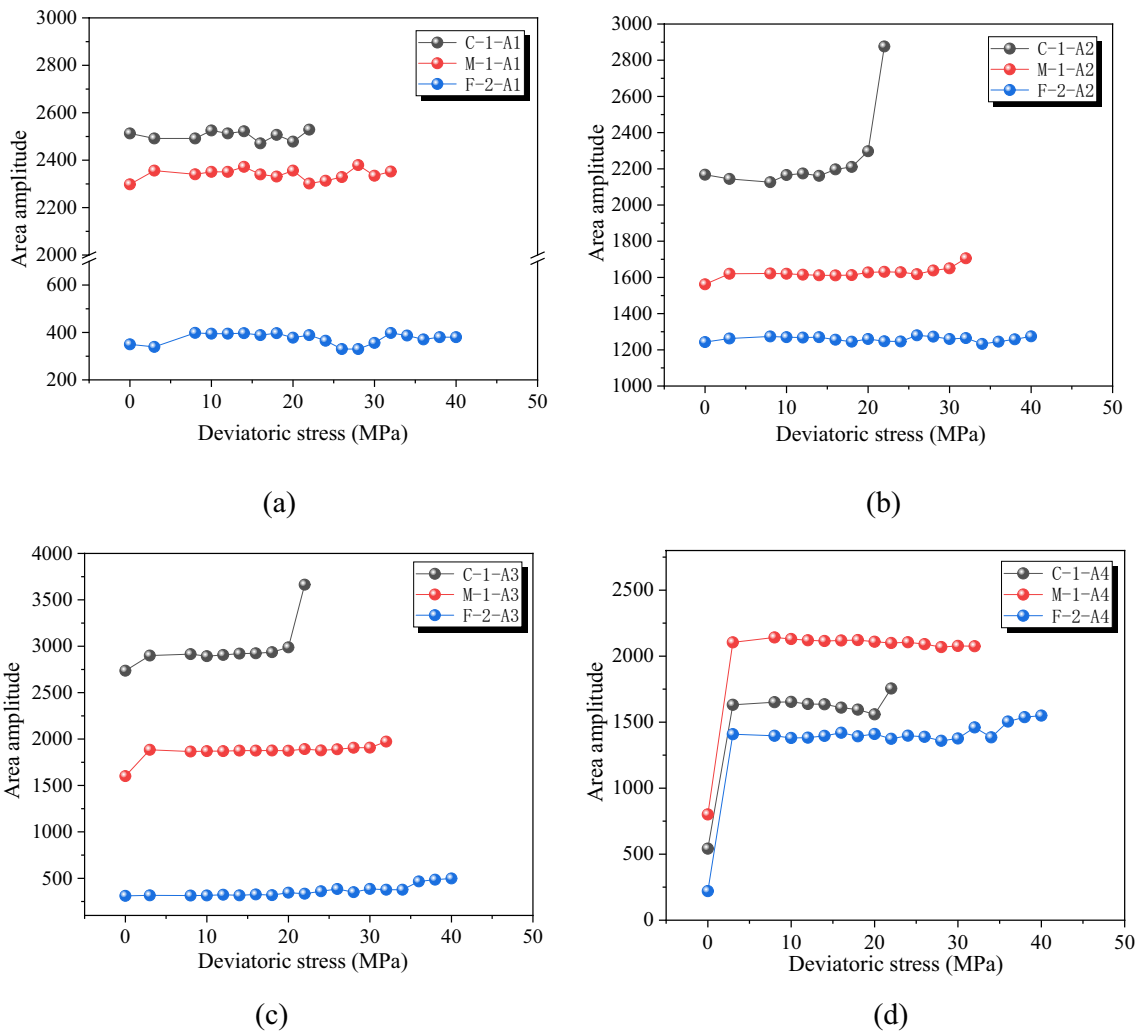
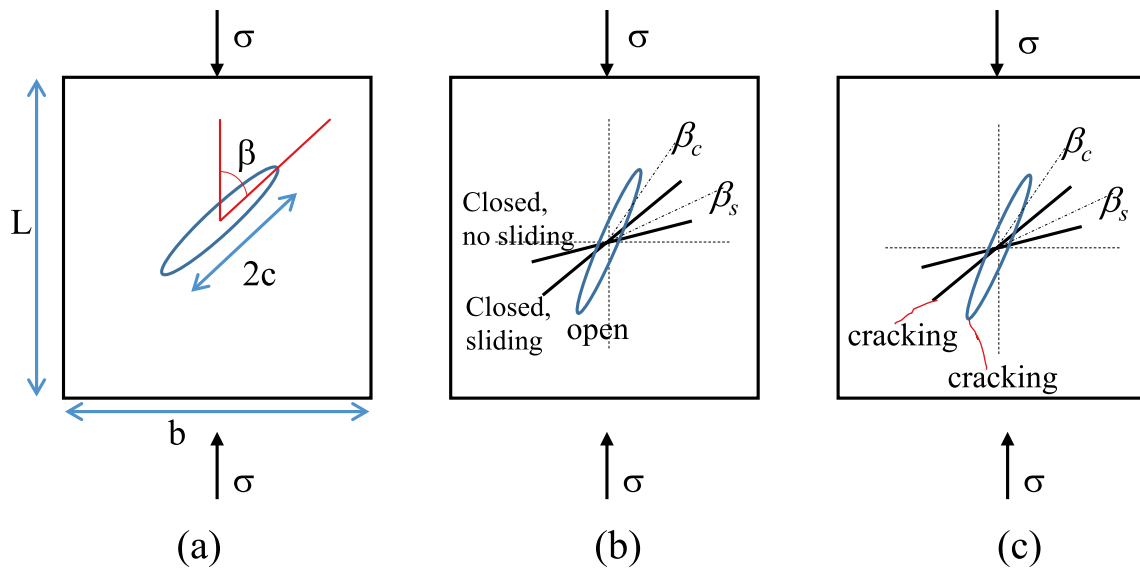


Fig. 5 Relationship between deviatoric stress and area amplitude for different sandstone: **a** micropores; **b** pores; **c** mesopores; **d** macropores



**Fig. 6** Rock body containing a single crack: **a** an elliptical crack whose plane makes an angle  $\beta$  with the direction of the loading stress (David et al. 2012); **b** The critical angles that delineate these three regimes; **c** damage evolution schematic diagram

If the crack is open and the plane in which the crack is located (not its normal vector) is inclined at an angle  $\beta$  with respect to the direction of the applied stress, then the excess energy assuming plane stress can be written as (David et al. 2012):

$$\Delta W_{open} = \frac{\pi \sigma^2 c^2 \sin^2(\beta)}{E} \tag{4}$$

If instead, plane strain conditions are assumed,  $E$  is replaced with  $E/(1 - \nu^2)$ , where  $\nu$  is the Poisson's ratio of the unfractured body. Because  $\nu$  did not appear in the case of plane stress, the effective modulus of the rock body containing one crack can be expressed as follows:

$$\frac{E}{E_{eff}} = 1 + 2(c^2/bL)\pi \sin^2(\beta) \tag{5}$$

When the crack closes, its opposing faces contact each other. If next they slide relative to each other, the energy supplied by the loading stress can be written as (David et al. 2012):

$$\Delta W_{slid} = \frac{\pi \sigma c^2}{E} (\tau - \tau_f) \sin(\beta) \cos(\beta) \tag{6}$$

In Eq. (6),  $\tau = \sigma \sin(\beta) \cos(\beta)$  represents the shear stress resolved along the crack plane, and  $\tau_f$  represents the frictional stress along the shear plane.

Finally, if the crack closes but no sliding occurs, it contributes nothing to the energy nor the elastic modulus (David et al. 2012). That is, the effective modulus is not affected by closed non-slipping cracks.

Furthermore, David et al. (2012) proposed a criterion for determining whether a crack is open or closed. The cracks are assumed to be elliptical with an initial aspect ratio (minor axis to major axis) of  $\alpha < 1$ . Under idealized conditions,  $\alpha = 0$ . The friction coefficient when the crack is closed is  $\mu$ .

We define the normal stress on the surface of the crack as the actual normal stress  $\sigma_n = \sigma \sin^2(\beta)$ , where  $\sigma_c$  is the normal stress that causes the crack to close and its surfaces to contact each other. When the crack remains open under compressive stress  $\sigma$ , then  $\sigma \sin^2(\beta) < \sigma_c$ . Hence, if  $\beta < \beta_c$ , the crack is open, and if  $\beta > \beta_c$ , the crack is closed. The critical crack angle  $\beta_c$  and critical crack angle when crack sliding occurs  $\beta_s$  can be expressed as:

$$\beta_c(\hat{\sigma}) = \arcsin \sqrt{1/\hat{\sigma}}, \quad \hat{\sigma} = \sigma/\sigma_c = 2\sigma/E\alpha \tag{7}$$

$$\beta > \beta_s = \frac{1}{2} \left[ \arccos \left\{ \frac{\mu [1 - (2/\hat{\sigma})]}{\sqrt{1 + \mu^2}} \right\} + \arctan \left( \frac{1}{\mu} \right) \right] \tag{8}$$

In natural rock materials, microcracks are typically randomly distributed. During the loading process, some cracks opened and some cracks closed, as shown in Fig. 6(b). When the load reached a certain degree, some cracks developed tensile and shear propagation, whereas other cracks did not develop. This phenomenon agrees with the variation of the T2-weighted spectrum of the three types of sandstone, as illustrated in Fig. 6c.

Sandstone is a type of sedimentary rock, composed of a variety of cemented sand grains, with grain diameters of 0.05–2 mm, in which the sand content is greater than 50%.

If sand grains composing the rock samples are taken as a system of random particles, then the different pore types, angles, and positions are randomly distributed in the rock samples. Combined with the above theory, it is proven that the pore distribution in sandstone increases significantly under low compression stress (Fig. 5). However, this stress stage is typically considered to correspond to the compaction state of the rock. This phenomenon does not fit the macroscopic stress-strain curve, but the physical properties of sandstone. This is because of the random distribution of microcracks or pores within the sandstone. Furthermore, the area of pores and mesopores increased with increasing deviatoric stress, whereas the area of macropores decreased. This indicates that the number of pores and mesopores increased, whereas the number of macropores decreased. To explain this phenomenon, we introduce the fracture process zone (FPZ) concept. Figure 7 shows typical load-displacement diagrams of the FPZ at different stages of damage evolution. The stress concentration at the crack tip leads to crack propagation; however, owing to the existence of the FPZ, the crack does not appear in the form of macropores but in the form of micropores or mesopores, forming a fracture zone at the crack tip. This further proves the pore-change law observed in this study.

### 3.3 Damage Mode of Sandstone Based on Real-Time NMR Technique

Based on Fig. 5, we know that the damage to sandstone during real-time loading mainly depends on the changes in the pores and mesopores. The increase in macropores is

simply a change in the opening. Hence, the damage evolution of sandstone is mainly influenced by the pores and mesopores. Then, the stress-strain relation can be divided into five stages based on the pore-changing law (shown in Fig. 5): pore opening, pore retention, pore compaction, pore growth, and post-peak.

Furthermore, the damage theory proposed by Kachanov points out that the main mechanism of material degradation is the decrease in the effective bearing area caused by defects or fractures in the material. The damage parameters can be expressed as (Kachanov 1958):

$$\phi = \bar{A}/A \quad (9)$$

where  $\phi$  is the continuum parameter representing the continuity of the rock samples,  $\bar{A}$  is the effective bearing area of the damaged rock samples, and  $A$  is the total area of the damaged rock samples.

Based on phenomenological macro statistical damage mechanics and the binary assumption of damaged and undamaged units, the macro damage phenomenon is regarded as the average effect of many microscopic damage units. Uneven micro damage is described by a normal or Weibull distribution, and the damage variable is defined from a macroscopic phenomenological perspective. A statistical constitutive model of rock damage under uniaxial and triaxial compression was established (Yang et al. 2004).

Based on this theory, Rabotnov introduced the damage variable  $D_n$  (Rabotnov 1963):

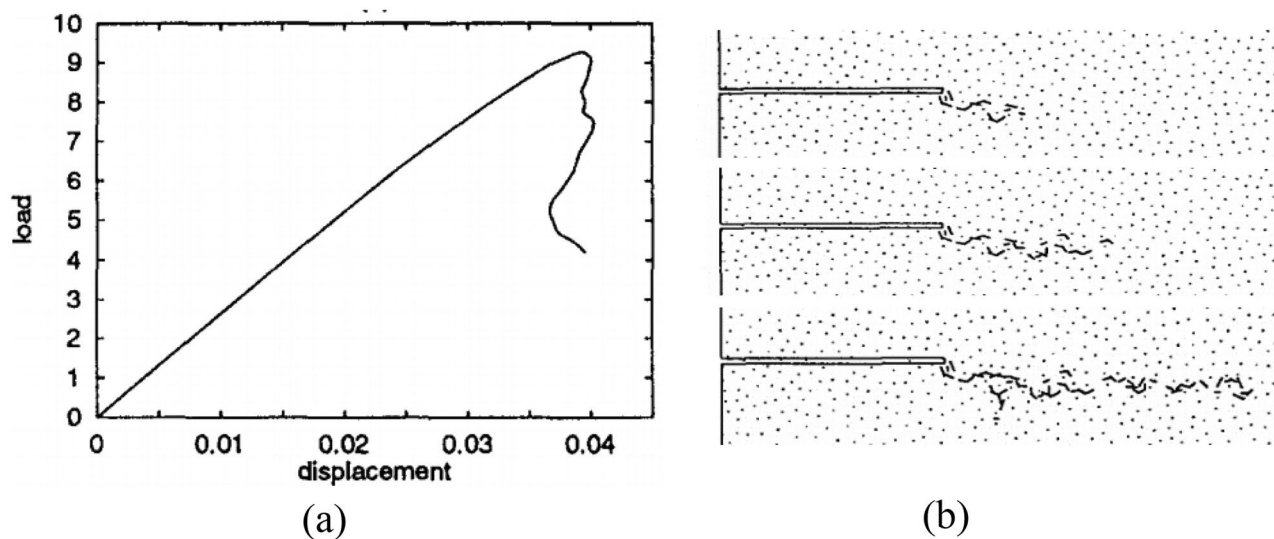


**Fig. 7** Load-displacement diagrams and Evolution of the FPZ (Jirasek and Bazant 1994): **a** Load-displacement diagram; **b** Evolution of the FPZ for a microductile material



$$D_n = \frac{nA_0}{kA_0} = \frac{n}{k} \tag{10}$$

where  $n$  is the number of damaged units,  $k$  is the total number of units in the rock sample, and  $A_0$  is the area of the damaged or undamaged units (which are equal), as shown in Fig. 8.

However, it is difficult to obtain the bearing area of the rock samples. Subsequently, many other damage variables are considered with basic rock parameters that can be easily obtained by researchers, such as density, porosity, sound velocity, elastic modulus, and volume (Jin et al. 2020; Meng et al. 2021). However, these physical quantities have significant errors in describing rock damage owing to measurement errors. Hence, using NMR to describe the variation of different pore areas to characterize rock damage is the main method used in this study. Furthermore, based on Eq. (10), the initial damage to the rock samples was considered.

Then, different T2-weighted spectral areas represent different pore contents, and the damage variable  $D_n$  can be rewritten as:

$$D_n = \frac{aA'_{micro} + bA'_{pore} + cA'_{meso} + dA'_{macro}}{aA_{micro} + bA_{pore} + cA_{meso} + dA_{macro}} - 1 \tag{11}$$

where  $a, b, c,$  and  $d$  represent the weights of micropores, pores, mesopores, and macropores in the initial rock samples, respectively,  $A_{micro}, A_{pore}, A_{meso},$  and  $A_{macro}$  represent the spectral areas of micropores, pores, mesopores, and macropores in the initial rock samples, respectively, and  $A'_{micro}, A'_{pore}, A'_{meso},$  and  $A'_{macro}$  represent the spectral areas of micropores, pores, mesopores, and macropores in the damaged rock samples, respectively.

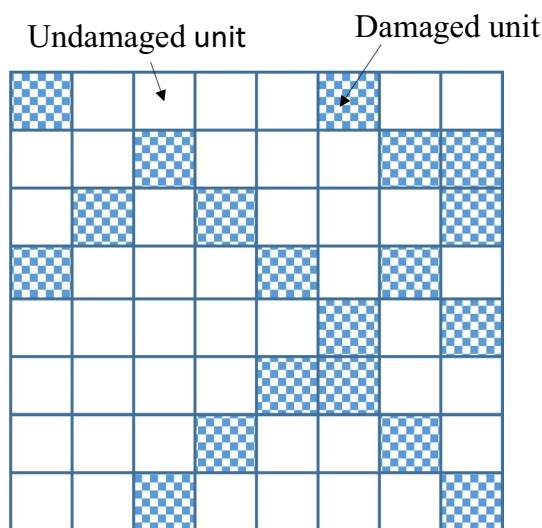


Fig. 8 Structure diagram of rock micro unit

Under different stress conditions, the variation coefficient of spectral area corresponding to pore sizes in sandstone is calculated as follows (Meng et al. 2021):

$$V_i = \frac{\sigma_i}{\bar{x}_i} \tag{12}$$

where  $V_i$  is the variation in the coefficient of the spectral area corresponding to micropores, pores, mesopores, and macropores,  $\sigma_i$  is the standard deviation of the spectral area corresponding to micropores, pores, mesopores, and macropores, and  $\bar{x}_i$  is the average value of the spectral area corresponding to micropores, pores, mesopores, and macropores.

With this method, a larger coefficient of variation can better reflect the differences in the evaluated units. The weights corresponding to  $a, b, c,$  and  $d$  are calculated as follows:

$$W_i = \frac{V_i}{\sum_i V_i} \tag{13}$$

In this study, the coefficients of variation of spectral area were calculated under compression conditions. The coefficients of variation of the spectral areas corresponding to the micropores, pores, mesopores, and macropores were 0.011, 0.091, 0.07, and 0.207, respectively, for sample C-1; 0.011, 0.013, 0.044, and 0.189, respectively, for sample M-1; 0.062, 0.01, 0.217, and 0.268, respectively, for sample F-2; 0.028, 0.236, 0.197, and 0.539, respectively, for sample C-1; 0.042, 0.0496, 0.173, and 0.735, respectively, for sample M-1; and 0.111, 0.0186, 0.389, and 0.481, respectively, for sample F-1. However, based on the discussion in Sect. 3.2, the initial sharp increase in the spectral areas of the macropores is not a quantitative manifestation of rock damage. Therefore, a correction factor based on ignoring the rapidly increasing macropore spectral area is considered. When the rock sample failed under compression, the damage variable was  $D_n \leq 0$ . The revised weights of  $a, b, c,$  and  $d$  corresponding to the micropores, pores, mesopores, and macropores for the samples are listed in Table 2. The damage evolution curves for the different samples are plotted in Fig. 9.

As shown in Fig. 9, the damage variable exhibits a similar pattern to the T2 spectral area signal. The sharp increase resulted from the pore opening. Subsequently,  $D_n$  decreases first and begins to increase before the failure stage. When the sample was fractured,  $D_n$  exhibited an obvious increase owing to the development of macroscopic cracks. This is because a large number of macroscopic cracks develop along with micro- and medium-sized cracks, resulting in a rapid increase in the damage value of the rock samples at the last stage of loading.

**Table 2** Weights of *a*, *b*, *c* and *d* of corresponding to micropores, pores, mesopores and macropores

Sample	<i>a</i>	<i>b</i>	<i>c</i>	<i>d</i>
C-1	0.0512	0.4372	0.3647	0.1467
M-1	0.1214	0.2222	0.5249	0.1314
F-2	0.1590	0.0290	0.6615	0.1502

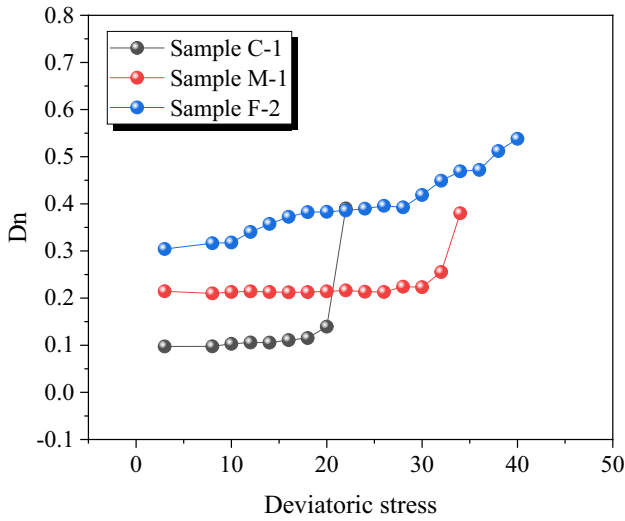


**Fig. 9** Damage evolution curves of different samples

### 3.4 Fracture of Sandstone

Figure 10 shows the stress-strain curves of the tested sandstone samples during the entire loading process. Four stages are identified in these curves: compaction, linear deformation, elastic-plastic, and post-peak. These are different from the loading stages found in real-time NMR scans based on the pore-changing law: pore opening, pore retention, pore

compaction, pore growth, and post-peak. This indicates that in the entire process of the rock compression test, the changes in the microscopic pore structure are quite different from those in the macroscopic stress-strain response, particularly during the initial stage of pore expansion and the compaction stage of macroscopic stress-strain response. Moreover, the peak strength of the sandstone samples ranged from 24.8 MPa for sample C-1 to 42.6 MPa for sample F-2, owing to the differences in pore structure and mineral content.

MRI and fracture images of the sandstone samples were obtained during the loading process. Figure 11 shows the failure modes of the tested sandstone samples under triaxial compression loading. The failure mode varied from tensile to shear failure for coarse and fine sandstone samples, respectively. MRI images prior to loading display no obvious fractures in the samples but a large number of micropores. Furthermore, the MRI images showed different pore distributions. The finer the sandstone, the sparser the MRI image point in Fig. 11. The main fracture in the coarse sandstone sample was a tensile fracture in the middle of the sample. The main fracture in the medium-coarse sandstone sample initiated from the side of the sample and formed symmetrical shear cracks. In the fine sandstone sample, the main fracture formed evident local shear cracks at the ends of the sample. This indicates that the micropore structure has a significant influence on the failure mode of sandstone during low-confining-pressure triaxial compression tests.

### 4 Conclusions

In this study, real-time T2-weighted NMR spectra and images of different types of sandstone samples were obtained using an NMR test system equipped with a loading device. The following are the main conclusions that can be drawn from the test results:

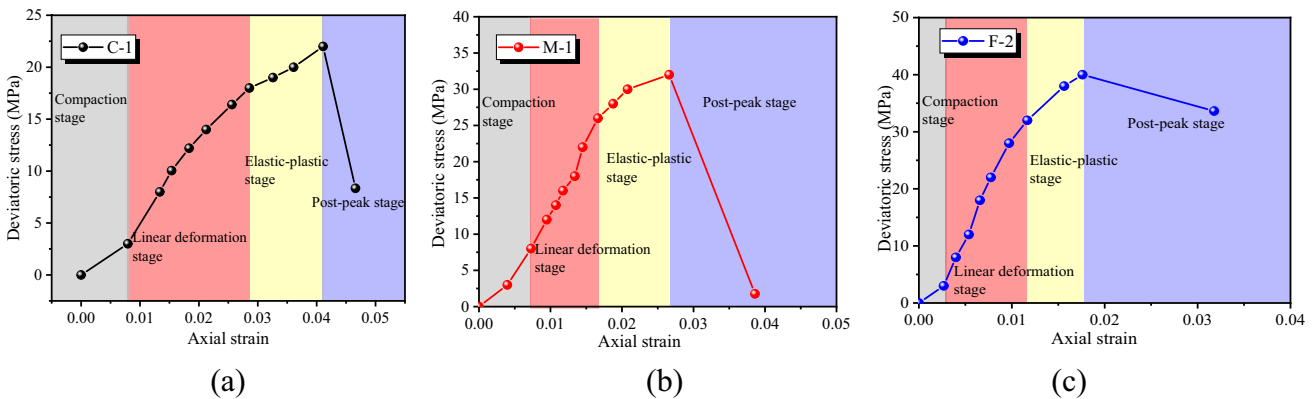


**Fig. 10** Relationship between deviatoric stress and strain of sandstone samples: **a** sample C-1; **b** sample M-1; **c** sample F-2

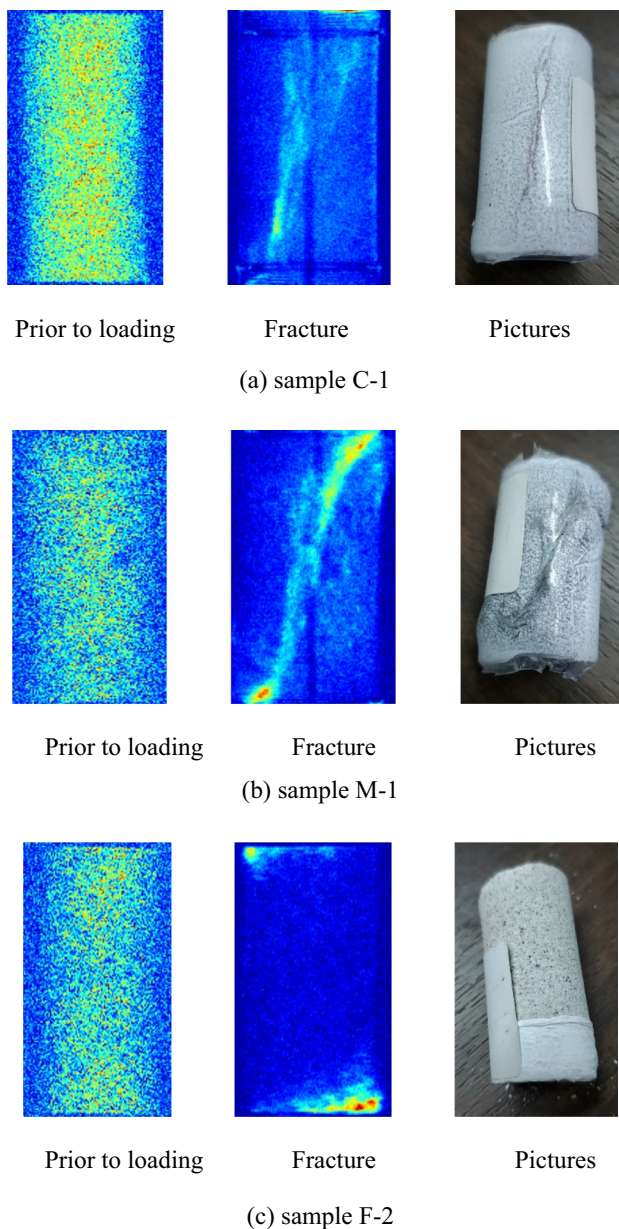


**Fig. 11** Failure modes of the tested sandstone samples under triaxial compression loading

- (1) In contrast to the other three pore conditions, the area of macropores in the three different sandstones significantly increased during the initial loading stage and then started decreasing as the loading stress increased. However, they played an opposite role in the damage evolution process, resulting in a phenomenon that is contrary to our expectations and providing a new basis for understanding rock damage evolution.
- (2) The distribution of pores in the sandstone samples significantly increased under low-compression-stress

conditions. However, this stress stage is typically considered to be the compaction stage of the rock. This phenomenon does not fit the macroscopic stress-strain curve, but the physical properties of sandstone. This is because of the random distribution of microcracks and pores within the sandstone. Furthermore, the area of the pores and mesopores increased with increasing deviatoric stress, whereas the area of macropores decreased. This indicates that, as loading progressed, the number of pores and mesopores increased, whereas the number of macropores decreased.

- (3) A damage model based on the NMR results was proposed. The damage variable  $D_n$  shows a pattern similar to that of the T2 spectral area signal. An initial sharp increase resulted from the opening of the pores. Subsequently,  $D_n$  decreased and then began to increase again before the failure stage. When the sample fractured,  $D_n$  exhibited an evident increase owing to the development of macroscopic cracks.
- (4) The main failure mechanisms in the coarse, medium-coarse, and fine sandstone samples were, respectively, a tensile fracture in the middle of the sample, symmetrical shear cracks initiated from the side of the sample, and local shear cracks at the ends of the sample. This indicates that the structure of the micropores has a considerable influence on the failure mode of sandstone during low-confining-pressure triaxial compression tests.

**Acknowledgements** This work was supported by National Natural Science Foundation of China (52164001, 52064006, 52004072), Guizhou Provincial Science and Technology Projects (No. [2020]2004), Science and Technology Support Project of Guizhou ([2020]4Y044), [2021]N404 and [2021]N511), Cultivation Program of Guizhou University ([2020] No. 1), Talents of Guizhou University (Grant No. 201901), the Special Research Funds of Guizhou University (Grant No. 201903, 202011, 202012).

**Data availability** The data that support the findings of this study are available on request from the corresponding author, upon reasonable request.

## Declarations

**Conflict of interest** The authors declare that they have no conflicts of interest to this work. The authors also declare that they do not have any commercial or associative interest that represents a conflict of interest in connection with the work submitted.

## References

- Bi J, Liu PF, Gan F (2020) Effects of the cooling treatment on the dynamic behavior of ordinary concrete exposed to high temperatures. *Constr Build Mater* 248:118688

- Bi J, Tang JC, Wang CL, Quan DG, Teng MY (2022) Crack coalescence behavior of rock-like specimens containing two circular embedded flaws. *Lithosphere*. (Special 11):9498148. <https://doi.org/10.2113/2022/9498148>
- Cai Y, Liu D, Pan Z (2013) Petrophysical characterization of Chinese coal cores with heat treatment by nuclear magnetic resonance. *Fuel* 108(11):292–302
- Carette J, Staquet S (2016) Monitoring the setting process of eco-binders by ultrasonic P-wave and S-wave transmission velocity measurement: mortar vs concrete. *Constr Build Mater* 110:32–41
- Cheng H, Zhou XP, Pan XK, Berto F (2021) Damage analysis of sandstone during the creep stage under the different levels of uniaxial stress using NMR measurements. *Fatigue Fract Eng Mater Struct* 44:719–732
- David EC, Brantut N, Schubnel A, Zimmerman RW (2012) Sliding crack model for nonlinearity and hysteresis in the uniaxial stress–strain curve of rock. *Int J Rock Mech Min* 52:9–17
- De Castro AR, Agnaou M, Ahmadi-S´enichault A, Omari A (2020) Numerical porosimetry: evaluation and comparison of yield stress fluids method, mercury intrusion porosimetry and pore network modelling approaches. *Comput Chem Eng* 133:106662
- Dunn KJ, Bergman DJ, Latorraca GA (2002) Nuclear magnetic resonance: petrophysical and logging applications. Elsevier, New York
- Fahimifar A, Zareifard MR (2014) A new elasto-plastic solution for analysis of underwater tunnels considering strain-dependent permeability. *Struct Infrastruct E* 10(11):1432–1450
- Fang WC, Jiang HQ, Li J, Li W, Li JJ, Zhao L, Feng XN (2016) A new experimental methodology to investigate formation damage in clay-bearing reservoirs. *J Pet Sci Eng* 143:226–234
- Fang X, Xu J, Wang P (2018) Compressive failure characteristics of yellow sandstone subjected to the coupling effects of chemical corrosion and repeated freezing and thawing. *Eng Geol* 233:160–171
- Frosch GP, Tillich JE, Haselmeier R, Holz M, Althaus E (2000) Probing the pore space of geothermal reservoir sandstones by nuclear magnetic resonance. *Geothermics* 29:671–687
- Hodot B (1966) Outburst of coal and coalbed gas (Chinese translation). China Coal Industry Press, Beijing
- Huang QM, Liu SM, Wu B, Wang G, Li GF, Guo ZG (2021) Role of VES-based fracturing fluid on gas sorption and diffusion of coal: an experimental study of Illinois basin coal. *Process Saf Environ* 148:1243–1253
- Jaeger JC, Cook NGW, Zimmerman RW (2007) Fundamentals of rock mechanics, 4th edn. Wiley-Blackwell, Oxford
- Jia H, Ding S, Zi F, Dong Y, Shen Y (2020) Evolution in sandstone pore structures with freeze-thaw cycling and interpretation of damage mechanisms in saturated porous rocks. *Catena* 195:104915
- Jin P, Hu Y, Shao J, Liu Z, Feng G, Song S (2020) Influence of temperature on the structure of pore–fracture of sandstone. *Rock Mech Rock Eng* 53(1):1–12
- Jirasek M, Bazant ZP (1994) Macroscopic fracture characteristics of random particle systems. *Int J Fracture* 69(3):201–228
- Kachanov LM (1958) On the creep fracture time. *Tekhnicheskich Nauk* 8:26–31
- Kou M, Liu X, Wang Z, Tang S (2021) Laboratory investigations on failure, energy and permeability evolution of fissured rock-like materials under seepage pressures. *Eng Fract Mech* 247:107694
- Li JL, Kaunda RB, Zhu LY, Zhou KP, Gao F (2019) Experimental study of the pore structure deterioration of sandstones under freeze-thaw cycles and chemical erosion. *Adv Civ Eng*. <https://doi.org/10.1155/2019/9687843>
- Li M, Wang D, Shao Z (2020) Experimental study on changes of pore structure and mechanical properties of sandstone after high-temperature treatment using nuclear magnetic resonance. *Eng Geol* 275:105739
- Liu JP, Li YH, Xu SD, Sa Xu, Jin CY (2015) Cracking mechanisms in granite rocks subjected to uniaxial compression by moment tensor analysis of acoustic emission. *Theor Appl Fract Mech* 75:151–159
- Matteson A, Tomanic JP, Herron MM, Allen DF, Kenyon WE (2000) NMR relaxation of clay/brine mixtures. *Spe Reserv Eval Eng* 3:602–603
- Meng T, Liu R, Meng X (2019) Evolution of the permeability and pore structure of transversely isotropic calcareous sediments subjected to triaxial pressure and high temperature. *Eng Geol* 253:27–35
- Meng F, Zhai Y, Li Y, Zhao R, Li Y, Gao H (2021) Research on the effect of pore characteristics on the compressive properties of sandstone after freezing and thawing. *Eng Geol* 286:106088
- Munoz H, Taheri A (2017) Local damage and progressive localisation in porous sandstone during cyclic loading. *Rock Mech Rock Eng* 50(12):3253–3259
- Rabotnov YN (1963) On the equations of state for creep. In: Koiter WT (ed) Progress in applied mechanics, Prager Anniversary Volume. McMillan, New York, p 307–315
- Rodriguez P, Arab PB, Celestino TB (2016) Characterization of rock cracking patterns in diametral compression tests by acoustic emission and petrographic analysis. *Int J Rock Mech Min Sci* 83:73–85
- Sun H, Sun Q, Deng W, Zhang W, Lü C (2017) Temperature effect on microstructure and P-wave propagation in Linyi sandstone. *Appl Therm Eng* 115:913–922
- Sun B, Zhu ZD, Shi C, Luo ZH (2017) Dynamic mechanical behavior and fatigue damage evolution of sandstone under cyclic loading. *Int J Rock Mech Min* 94:82–89
- Tang ZQ, Zhai C, Zou QL, Qin L (2016) Changes to coal pores and fracture development by ultrasonic wave excitation using nuclear magnetic resonance. *Fuel* 186:571–578
- Wei J, Zhang L, Li B, Wen Z (2019) Non-uniformity of coal damage caused by liquid nitrogen freeze-thaw. *J Nat Gas Sci Eng* 69:102946
- Weng L, Wu Z, Liu Q, Chu Z, Zhang S (2021) Evolutions of the unfrozen water content of saturated sandstones during freezing process and the freeze-induced damage characteristics. *Int J Rock Mech Min Sci* 142:104757
- Westphal H, Surholt I, Kiesl C, Thern HF, Kruspe T (2005) NMR measurements in carbonate rocks: problems and an approach to a solution. *Pure Appl Geophys* 162:549–570
- Yang SQ, Xu WY, Wei LD, Su CD (2004) Statistical constitutive model for rock damage under uniaxial compression and its experimental study. *J Hohai Univ (Nat Sci)* 32(2):200–203
- Yin D, Xu Q (2021) Investigating the damage evolution of sandstone using electrical impedance spectroscopy. *Int J Rock Mech Min Sci* 144:104817
- Zhai C, Yu X, Xiang X (2015) Experimental study of pulsating water pressure propagation in CBM reservoirs during pulse hydraulic fracturing. *J Nat Gas Sci Eng* 25:15–22
- Zhang J, Zhou X (2020) AE event rate characteristics of flawed granite: from damage stress to ultimate failure. *Geophys J Int* 222(2):795–814
- Zhang JZ, Zhou XP (2020) Forecasting catastrophic rupture in brittle rocks using precursory AE time series. *J Geophys Res Solid Earth*. <https://doi.org/10.1029/2019JB019276>
- Zhang YL, Sun Q, He H, Cao LW, Zhang WQ, Wang B (2017) Pore characteristics and mechanical properties of sandstone under the influence of temperature. *Appl Therm Eng* 113:537–543
- Zhao HT, Qin X, Liu JP (2018) Pore structure characterization of early-age cement pastes blended with high-volume fly ash. *Constr Build Mater* 189:934–946
- Zhao HT, Ding J, Huang YY, Xu GD, Li W, Zhang SP, Wang PG (2020) Investigation on sorptivity and capillarity coefficient of

- mortar and their relationship based on microstructure. *Constr Build Mater* 265:120332
- Zhao Y, Bi J, Wang CL, Liu PF (2021) Effect of unloading rate on the mechanical behavior and fracture characteristics of sandstones under complex triaxial stress conditions. *Rock Mech Rock Eng* 54(9):4851–4866
- Zhao Y, Wang C, Ning L, Bi J (2022) Pore and fracture development in coal under stress conditions based on nuclear magnetic resonance and fractal theory. *Fuel* 309:122112
- Zheng Y, Chen C, Liu T, Ren Z (2021) A new method of assessing the stability of anti-dip bedding rock slopes subjected to earthquake. *B Eng Geol Environ* 80(5):3693–3710
- Zhou XP, Bi J, Deng RS (2019) Effects of brittleness on crack behaviors in rock-like materials. *J Test Eval* 4(48):2829–2851
- Zhou Y, Wu Z, Weng L, Liu Q (2021) Seepage characteristics of chemical grout flow in porous sandstone with a fracture under different temperature conditions: An NMR based experimental investigation. *Int J Rock Mech Min Sci* 142:104764
- Zuo J, Xie H, Zhou H, Peng S (2007) Experimental research on thermal cracking of sandstone under different temperature. *Chin J Geophys* 50:1150–1155

**Publisher's Note** Springer Nature remains neutral with regard to jurisdictional claims in published maps and institutional affiliations.

Springer Nature or its licensor (e.g. a society or other partner) holds exclusive rights to this article under a publishing agreement with the author(s) or other rightsholder(s); author self-archiving of the accepted manuscript version of this article is solely governed by the terms of such publishing agreement and applicable law.